A Melting-Layer Model for Passive/Active Microwave Remote Sensing Applications. Part I: Model Formulation and Comparison with Observations

WILLIAM S. OLSON,* PETER BAUER,+ NICOLAS F. VILTARD,# DANIEL E. JOHNSON,@ WEI-KUO TAO,& ROBERT MENEGHINI,& AND LIANG LIAO**

*Joint Center for Earth Systems Technology, University of Maryland, Baltimore County, Baltimore, Maryland
+Deutsche Forschungsanstalt für Luft- und Raumfahrt, Cologne, Germany
#Centre d'Etudes des Environnements Terrestre et Planetaires, Velizy, France
@Science Systems and Applications, Inc., Lanham, Maryland
&NASA Goddard Space Flight Center, Greenbelt, Maryland
**Caelum Research Corporation, Rockville, Maryland

(Manuscript received 11 March 2000, in final form 30 October 2000)

ABSTRACT

In this study, a 1D steady-state microphysical model that describes the vertical distribution of melting precipitation particles is developed. The model is driven by the ice-phase precipitation distributions just above the freezing level at applicable grid points of ''parent'' 3D cloud-resolving model (CRM) simulations. It extends these simulations by providing the number density and meltwater fraction of each particle in finely separated size categories through the melting layer. The depth of the modeled melting layer is primarily determined by the initial material density of the ice-phase precipitation. The radiative properties of melting precipitation at microwave frequencies are calculated based upon different methods for describing the dielectric properties of mixed-phase particles. Particle absorption and scattering efficiencies at the Tropical Rainfall Measuring Mission Microwave Imager frequencies (10.65–85.5 GHz) are enhanced greatly for relatively small (~0.1) meltwater fractions. The relatively large number of partially melted particles just below the freezing level in stratiform regions leads to significant microwave absorption, well exceeding the absorption by rain at the base of the melting layer. Calculated precipitation backscatter efficiencies at the precipitation radar frequency (13.8 GHz) increase with particle meltwater fraction, leading to a ''bright band'' of enhanced radar reflectivities in agreement with previous studies. The radiative properties of the melting layer are determined by the choice of dielectric models and the initial water contents and material densities of the ''seeding'' ice-phase precipitation particles. Simulated melting-layer profiles based upon snow described by the Fabry–Szyrmer core-shell dielectric model and graupel described by the Maxwell-Garnett water matrix dielectric model lead to reasonable agreement with radar-derived melting-layer optical depth distributions. Moreover, control profiles that do not contain mixed-phase precipitation particles yield optical depths that are systematically lower than those observed. Therefore, the use of the melting-layer model to extend 3D CRM simulations is likely justified, at least until more-realistic spectral methods for describing melting precipitation in high-resolution, 3D CRMs are implemented.

1. Introduction

Several methods for estimating instantaneous precipitation rates from spaceborne passive microwave radiometer measurements have been developed and applied with moderate success (Smith et al. 1994). In recent years, these rainfall retrieval methods have been primarily applied to observations of the Special Sensor Microwave Imager (SSM/I), a component of several of the Defense Meteorological Satellite Program's polar-orbiting platforms. Intercomparisons of the methods have demonstrated the utility of physically based rainfall algorithms, which rely on physical models relating the three-dimensional structure of precipitating clouds to the upwelling radiances measured by the SSM/I (see Ebert and Manton 1998). The launch of the Tropical Rainfall Measuring Mission (TRMM) Microwave Imager (TMI) in November of 1997 improved upon the capability of SSM/I by extending the channel frequency range (10.65–85.5 GHz) and resolution (5-km minimum footprint). In addition, a 13.8-GHz weather radar called the precipitation radar (PR) was included on the TRMM platform to provide detailed vertical structure (250-m resolution) of the observed precipitation.

By extending the passive radiometer physical models to include a description of the radar response to precipitation, retrieval procedures combining both radiometer and radar observations are achieved. Such physically based methods have already been developed and applied to TMI and PR data (e.g., Haddad et al. 1997).

Corresponding author address: William S. Olson, Joint Center for Earth Systems Technology, NASA Goddard Space Flight Center, Code 912, Greenbelt, MD 20771.
E-mail: olson@agnes.gsfc.nasa.gov

However, the physical models supporting these retrieval methods do not include an explicit representation of melting precipitation particles, which have an important radiative effect in stratiform rain regions.

Previous studies by Schols et al. (1997), Meneghini and Liao (1996, 2000), and Bauer et al. (1999) have indicated the possibility of significant absorption of microwaves by partially melted particles, in addition to the commonly observed enhanced radar reflectivity of the melting layer. Although the high radar reflectivities of melting hydrometeors typically occupy only a thin layer (~500 m), and thus might be ignored, the microwave absorption within the melting layer has more serious consequences for both radiometric and radar remote sensing of stratiform precipitation. Absorption and emission of microwaves by the melting layer might account for a significant portion of the emission observed by spaceborne passive radiometers—emission that might otherwise be attributed to liquid precipitation in physically based retrieval methods. Likewise, the two-way path attenuation of radar pulses by the melting layer must be included in calculations of the total attenuation of reflectivities measured by spaceborne radar.

In the current study, a one-dimensional, steady-state microphysical model of melting ice hydrometeors is developed, following the work of Bauer et al. (2000). Although simplified, the model yields the volume fractions of ice, air, and liquid water of melting particles of all species and sizes at a fine grid spacing in the vertical. This model is used in the manner of a parameterization to describe the vertical distribution of melting precipitation at applicable horizontal grid points of fully three-dimensional cloud-resolving model (CRM) simulations. This differs from previous melting parameterizations in that a more complete model of the melting process, including meltwater evaporation, particle interactions, and the effect of changing particle density on fall speed, is considered.

The dielectric and radiative properties of melting ice hydrometeors are calculated using different methods, and the results are intercompared. Extinction optical depth and reflectivity simulations are compared with the corresponding PR-derived quantities in an attempt to determine which modeling assumptions lead to simulations most consistent with the observations. Previous work (e.g., Fabry and Szyrmer 1999; Liao and Meneghini 2000) has focused on the consistency between modeled and observed reflectivities, but consistency between modeled and observed extinction is arguably more important for satellite remote sensing applications.

2. Model description

a. Microphysics of the melting model

Calculation of the electromagnetic properties of the melting layer requires, at the very least, a specification of the volume fractions of ice, air, and liquid of each melting particle within the ensemble of particles that compose the layer. From these volume fractions, the dielectric properties of the particles may be computed according to different approximate formulas (see section 2c). In addition, accurate simulations of upwelling radiances from cloud and precipitation distributions require that these distributions be specified in three dimensions at a resolution greater than 12 km in the horizontal, as indicated by Kummerow (1998). Such fields can be obtained from 3D CRM simulations; however, the microphysical schemes utilized in CRMs typically do not contain an explicit description of partially melted precipitation particles given the large computational requirements (e.g., Lin et al. 1983; Rutledge and Hobbs 1983, 1984). Also, it will be shown in section 2d that the height variation of melting-particle radiative properties is significant on scales of about 50 m, which is usually a much finer resolution than that provided by many CRMs. Therefore, in this study a one-dimensional melting-layer model is developed to describe the melting process at applicable horizontal grid points of a ''parent'' 3D CRM simulation.

The melting model described in this study is only applicable to regions in which updrafts and downdrafts are relatively weak in the vicinity of the freezing level. Under these conditions, precipitation will fall steadily through the air column, and only melting, sublimation/deposition, evaporation/condensation, and collection of particles need to be considered. Each grid point of the parent-model domain is first examined to find the maximum magnitude of the vertical velocity in the layer between the freezing level and 2 km below it. If the magnitude of the vertical velocity does not exceed 0.5 m s^{-1} in this layer and if ice-phase precipitation exists just above the freezing level, then the 1D melting model is applied to the grid point in question.

The temperature, relative humidity, vertical air motion, and hydrometeor fields at each qualified grid point from the parent 3D CRM simulation are first interpolated to the 50-m-resolution melting-model vertical grid (see Fig. 1). The top of the melting-model domain is assumed to coincide with the parent-model grid level at, or just above, the 0°C level, and the bottom of the model domain is set at 3 km below this level.

The size distributions of precipitation species (rain, snow, graupel) in the melting model are represented by number densities $n(i, z)$ at particle diameter intervals ΔD of 0.1 mm. The index i indicates the particle diameter interval, and z is the depth below the model top. A particle of a given size is characterized by its ice mass $m_{\text{ice}}(i, z)$, liquid water mass $m_{\text{liq}}(i, z)$, and volume of air $V_{\text{air}}(i, z)$.

At the top of the melting-model domain the particle size distributions and composition are inherited from the parent model; therefore,

$$n(i, 0) = n_{\text{init}}(D_{\text{init}_i}), \tag{1}$$

where $n_{\text{init}}(D_{\text{init}_i})$ is the parent-model particle number

density at the top of the melting-model domain for an initial particle diameter D_{init_i}. Ice precipitation species initially are assumed to be spherical and dry mixtures of ice and air (no meltwater or collected water); therefore, the masses of ice and liquid in a given particle are

$$m_{\text{ice}}(i, 0) = \begin{cases} \rho_m(D_{\text{init}_i})\dfrac{\pi D_{\text{init}_i}^3}{6}, & \text{ice species} \\ 0, & \text{rain} \end{cases} \quad (2)$$

and

$$m_{\text{liq}}(i, 0) = \begin{cases} 0, & \text{ice species} \\ \rho_{\text{liq}}\dfrac{\pi D_{\text{init}_i}^3}{6}, & \text{rain,} \end{cases} \quad (3)$$

where $\rho_m(D_{\text{init}_i})$ is the initial ice particle material density, which may be a function of diameter, and ρ_{liq} is the density of liquid water, 1.0 g cm^{-3}. The small mass of air in the particle is neglected, but the volume of air within the particle can be calculated from

$$V_{\text{air}}(i, 0) = \begin{cases} \dfrac{\pi D_{\text{init}_i}^3}{6}\left[\dfrac{\rho_{\text{ice}} - \rho_m(D_{\text{init}_i})}{\rho_{\text{ice}}}\right], & \text{ice species} \\ 0, & \text{rain} \end{cases} \quad (4)$$

where ρ_{ice} is the density of pure ice, 0.917 g cm^{-3}. In the discussion to follow, the diameter index i and level argument z have been omitted unless they are required for clarity.

A particle of a given diameter D is assumed to fall at a terminal velocity given by

$$w_T = -\left(\frac{4\rho_m g}{3\rho_a C_D}\right)^{1/2} D^{1/2} \quad (5)$$

where ρ_m is the material density of the particle,

$$\rho_m = \frac{m_{\text{ice}} + m_{\text{liq}}}{\dfrac{m_{\text{ice}}}{\rho_{\text{ice}}} + \dfrac{m_{\text{liq}}}{\rho_{\text{liq}}} + V_{\text{air}}}, \quad (6)$$

g is the acceleration of gravity, ρ_a is the density of air, and C_D is the particle drag coefficient. Because the parent-model simulations may have different fall speed formulations, the drag coefficient C_D is determined such that the total mass flux of a given ice (rain) species is equal to the mass flux of that species in the parent model at the top (bottom) of the melting-model domain. The drag coefficient of each hydrometeor species is assumed to be independent of particle size or melted fraction, and a completely melted ice particle assumes the drag coefficient of rain. The parameterization given in (5) for terminal velocity is used because the material density of an ice particle may change as the particle melts, and (5) accounts for the change in terminal velocity as a function of particle density.

As an ice or melting precipitation particle falls from level z to level $z - \Delta z$, the changes of the masses of ice and meltwater, and the volume of air in the particle are given by, respectively,

$$m_{\text{ice}}(i, z - \Delta z) = m_{\text{ice}}(i, z) + \left[-\delta\left(\frac{dm_{\text{melt}}}{dt}\right) - (1 - \delta)\left(\frac{dm_{\text{sub}}}{dt}\right) + \frac{dm_{\text{iacc}}}{dt}\right]\Delta t, \quad (7)$$

$$m_{\text{liq}}(i, z - \Delta z) = m_{\text{liq}}(i, z) + \delta\left(\frac{dm_{\text{melt}}}{dt} - \frac{dm_{\text{mevap}}}{dt} + \frac{dm_{\text{lacc}}}{dt}\right)\Delta t, \quad (8)$$

and

$$V_{\text{air}}(i, z - \Delta z) = V_{\text{air}}(i, z) + \left[\delta\left(\frac{dV_{\text{am}}}{dt}\right) + (1 - \delta)\left(\frac{dV_{\text{asd}}}{dt}\right) + \frac{dV_{\text{aacc}}}{dt}\right]\Delta t, \quad (9)$$

where

$$\Delta t = -\Delta z/(w_T + w), \quad \text{and} \quad (10)$$

$$\delta = \begin{cases} 0, & T < 273.16 \text{ K} \\ 1, & T \geq 273.16 \text{ K.} \end{cases} \quad (11)$$

Here, Δt is the time required for the particle to fall to the next level, and w is the vertical air velocity of the particle environment. For raindrops,

$$m_{\text{liq}}(i, z - \Delta z) = m_{\text{liq}}(i, z) + \left(-\frac{dm_{\text{revap}}}{dt}\right)\Delta t, \quad (12)$$

which governs both completely melted ice particles and raindrops from the parent simulation that are present at the top of the melting-model domain.

In the model, the processes of melting, sublimation/deposition, evaporation, and collection contribute to changes in the masses of ice and liquid and the volume of air in the falling particles, as seen on the right-hand sides of (7), (8), (9), and (12). The rate of increase of the mass of meltwater contained in the particle is determined by

$$\frac{dm_{\text{melt}}}{dt} = \begin{cases} (F_{\text{sens}} - F_{\text{evap}})/L_f, & T > 273.16 \text{ K}; \quad F_{\text{sens}} > F_{\text{evap}} \\ 0, & \text{otherwise.} \end{cases} \quad (13)$$

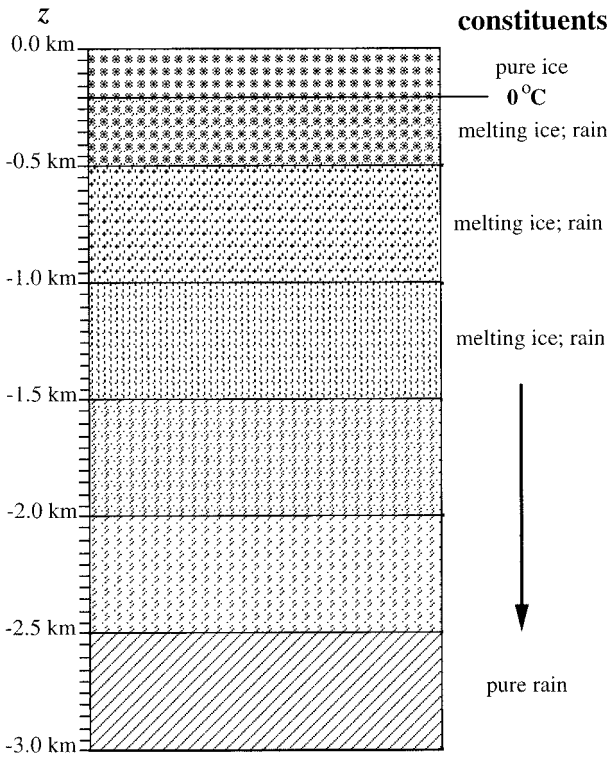

FIG. 1. Schematic of the grid domain of the 1D melting-layer model.

Here, F_{sens} is the rate of sensible heat transfer to the particle, F_{evap} is the rate of latent heat loss from the evaporation of meltwater, and L_f is the latent heat of fusion, 3.34×10^5 J kg^{-1}. Note that melting can only occur if the temperature of the particle environment exceeds 273.16 K and the rate of sensible heat transfer exceeds the rate of heat loss from evaporation. Equation (13) and the expressions for F_{sens} and F_{evap} follow the development of Ferrier (1994); however, collection terms that may also affect the particle heat balance are neglected.

The rate of sublimation/deposition of water vapor from/onto an ice particle's surface dm_{sub}/dt and the rates of evaporation of meltwater dm_{mevap}/dt and rain dm_{revap}/dt are also derived from Ferrier (1994). In the processes of melting or sublimation/deposition, it is assumed that the volume proportion of air to ice in a given ice or melting particle is maintained. Therefore, at temperatures above freezing,

$$\frac{dV_{am}}{dt} = -\frac{f_{ai}}{\rho_{ice}}\left(\frac{dm_{melt}}{dt}\right); \tag{14}$$

at subfreezing temperatures,

$$\frac{dV_{asd}}{dt} = -\frac{f_{ai}}{\rho_{ice}}\left(\frac{dm_{sub}}{dt}\right), \tag{15}$$

where

$$f_{ai} = \frac{V_{air}}{m_{ice}/\rho_{ice}} \tag{16}$$

is the volume ratio of air to ice in the particle.

In addition to phase-change processes, ice and melting particles can collide and combine to form composite particles, whereas pure liquid drops (rain) are immediately shed in collisions. Self-collection of raindrops is not considered here, given that this process is adequately represented in the parent models and the focus of this study is the evolution of melting precipitation particles. Which types of ice species may collect others or self-collect is determined by the microphysics of the parent-model simulation (see section 2b). Also, to maintain consistency with the original definitions of the particle species, a given particle can collect another particle only if its size is greater than the collected particle. This criterion ensures that the resulting composite particle has material properties closer to those of the collecting particle.

The rates of change of ice and liquid water mass of a single collecting particle are

$$\frac{dm_{iacc}(i)}{dt} = \sum_j m_{aice}(j)\frac{dN_a(j, i)}{dt}, \quad \text{and} \tag{17}$$

$$\frac{dm_{lacc}(i)}{dt} = \sum_j m_{aliq}(j)\frac{dN_a(j, i)}{dt}, \tag{18}$$

respectively. Also, the volume of air in the collecting and accreted particles is assumed to be conserved during collection; therefore

$$\frac{dV_{aacc}(i)}{dt} = \sum_j V_{aair}(j)\frac{dN_a(j, i)}{dt}. \tag{19}$$

Here, m_{aice} and m_{aliq} are the masses of ice and liquid water in each accreted particle, V_{aair} is the volume of air in the accreted particle, and the summations are over all accreted particles. The total number of particles with size index j accreted by a single collecting particle with size index i per unit time, $dN_a(j, i)/dt$, is given by the formula of Flatau et al. (1989).

The change in the number density of ice and melting precipitation particles is calculated in three steps. First, the reduction of particles by accretion is computed,

$$n(i, z - \Delta z)' = n(i, z) + \left[\frac{dn_a(i, z)}{dt}\right]\Delta t, \tag{20}$$

where the rate of change in the number density of accreted particles dn_a/dt is

$$\frac{dn_a(i, z)}{dt} = -\sum_j n_c(j, z)\frac{dN_a(i, j, z)}{dt}, \tag{21}$$

and n_c is the number density of collecting particles.

Next, $n(i, z - \Delta z)'$ is adjusted for the loss of particles due to evaporation or sublimation according to the governing equations (7)–(12). Because the melting model is steady state, the number flux of particles at level z,

TABLE 1. Characteristics of the parent 3D CRM simulations.

Model/simulation	Date	Approximate location	Horizontal/vertical resolution (km)	Grid dimensions	Duration
GCE/TOGA1	22 Feb 1993	9°S, 159°E	1.0/0.1–1.0	128 × 128 × 32	6 h
GCE/TOGA3	22 Feb 1993	9°S, 159°E	3.0/0.1–1.0	128 × 128 × 32	6 h
GCE/TOGA2	19 Dec 1992	2°S, 155°E	2.0/0.1–1.0	256 × 256 × 41	7 d
UW-NMS/COHMEX	11 Jul 1986	35°N, 87°W	1.0/0.5	51 × 51 × 42	4 h
UW-NMS/HURRICANE	11 Sep 1988	19°N, 70°W	3.3/0.4–0.8*	62 × 62 × 42*	6 h

* Refers to highest-resolution nested grid.

less the flux eliminated by accretion, evaporation, or sublimation, should equal the number flux of particles at the next level. This condition is satisfied if the number flux of ''surviving'' particles at z, $n(i, z - \Delta z)'[w_T(i, z) + w(z)]$, is set equal to the number flux at the next level, $n(i, z - \Delta z)[w_T(i, z - \Delta z) + w(z - \Delta z)]$. It follows that

$$n(i, z - \Delta z) = n(i, z - \Delta z)' \frac{[w_T(i, z) + w(z)]}{[w_T(i, z - \Delta z) + w(z - \Delta z)]}, \quad (22)$$

which yields the number density of particles at the next level. Note that $w_T(i, z - \Delta z)$ is obtained from (5) using the particle composition calculated at the next level.

The foregoing equations provide a description of the melting process that is sufficient for determining the bulk electromagnetic properties of the melting layer. However, because of differences in model physics and vertical resolution, as well as the lack of horizontal advection of precipitation into or out of the one-dimensional melting-model domain, the profiles of precipitation produced by the melting model may differ from those computed in the parent model. To help to correct for these differences, the size distribution of each precipitation particle species in the melting model is scaled, such that the total mass flux of the resulting precipitation distributions is equal to the parent-model total mass flux interpolated to the melting-model grid:

$$n_{\text{adj}}(i, z) = \gamma(z)\, n(i, z), \quad (23)$$

with the scaling factor

$$\gamma(z) = \sum_{\text{species}} M_{\text{par}}(z) \div \left\langle \sum_{\text{species}} \left\{ \sum_i n(i, z)[m_{\text{ice}}(i, z) + m_{\text{liq}}(i, z)] \times [w_T(i, z) + w(z)]\Delta D \right\} \right\rangle. \quad (24)$$

Here, $M_{\text{par}}(z)$ is the mass flux of a given precipitation species in the parent model interpolated to level z. From a theoretical perspective, the correction in (23) may seem heavy handed. However, the objective of the current work is to develop a description of the melting band with sufficient detail for radiative transfer calculations, and one that is compatible with the parent 3D model simulation, as opposed to a stand-alone model. In this sense, the melting model can be viewed as a local parameterization of processes not resolved by the parent model.

Last, from the computed ice and liquid masses and volume of air in a given particle, the volume fractions of ice, liquid, and air are calculated:

$$f_{\text{ice}}(i, z) = \frac{m_{\text{ice}}(i, z)/\rho_{\text{ice}}}{V(i, z)}, \quad (25)$$

$$f_{\text{liq}}(i, z) = \frac{m_{\text{liq}}(i, z)/\rho_{\text{liq}}}{V(i, z)}, \quad (26)$$

$$f_{\text{air}}(i, z) = \frac{V_{\text{air}}(i, z)}{V(i, z)}, \quad (27)$$

where

$$V(i, z) = \frac{m_{\text{ice}}(i, z)}{\rho_{\text{ice}}} + \frac{m_{\text{liq}}(i, z)}{\rho_{\text{liq}}} + V_{\text{air}}(i, z). \quad (28)$$

The quantities n_{adj}, f_{ice}, f_{liq}, and f_{air} are utilized in the following sections to calculate the electromagnetic properties of melting precipitation.

b. *Application to parent 3D cloud-resolving model simulations*

In the previous section, a simplified model describing the evolution of melting precipitation was developed. Being one-dimensional, this melting model is designed to represent the melting layer at a single grid point in a parent, 3D CRM simulation and is driven by the distributions of ice precipitation just above the freezing level in the parent simulation. In this section, the parent-model simulations are briefly described, and applications of the melting model to a single parent-model profile are presented. The 3D CRM runs serve as the basis of the melting simulations described in the following section, as well as the simulated radiance and radar reflectivity fields in Part II (Olson et al. 2001, this issue).

The parent-model simulations of this study are derived from the Goddard Cumulus Ensemble (GCE) model and the University of Wisconsin Nonhydrostatic Modeling System (UW-NMS; see Table 1). A detailed description of the GCE model may be found in Tao and

Simpson (1993). The GCE model is nonhydrostatic, with cloud microphysics described by an adaptation of the Lin et al. (1983) scheme. In this scheme, precipitating particle distributions are represented by inverse exponential distributions with fixed intercepts; the slopes of the distributions are adjusted to account for changes in water content, which are computed prognostically. The particle material densities in this scheme are also fixed: rain has a density of 1.0 g cm^{-3}; snow and graupel have densities of 0.1 and 0.4 g cm^{-3}, respectively. Graupel may collect snow in this scheme, but self-collection of snow or graupel is not included. Three GCE model simulations are utilized in the current work. Two of these simulations are initialized using temperature, humidity, and wind conditions observed on 22 February 1993, during the Tropical Ocean and Global Atmosphere Coupled Ocean–Atmosphere Response Experiment (TOGA COARE). A tropical squall line observed to the southwest of the TOGA COARE Intensive Flux Array (IFA) was simulated on a 1-km, 128 × 128 grid (TOGA1) and a 3-km, 128 × 128 grid (TOGA3). Both squall lines were initiated with a spreading cool pool centered in the model domain that generated a gust front–like forcing. A third simulation is derived from a long-term, forced simulation of convection in the TOGA COARE IFA during the period of 19–26 December 1992. The horizontally extensive mesoscale convective system that occurred on 24 December is simulated at 1200 UTC on a 2-km, 256 × 256 grid (TOGA2).

The UW-NMS is described in Tripoli (1992a). The microphysical scheme employed is from Flatau et al. (1989), with specified parameters tabulated by Panegrossi et al. (1998). In the simulations utilized in the current study, the precipitating hydrometeor species have inverse exponential size distributions, but, unlike the GCE model, the slopes of these distributions are fixed, while the intercepts are allowed to vary with water content. Rain and graupel have fixed material densities of 1.0 and 0.6 g cm^{-3} respectively, and snow has a size-dependent density given by

$$\rho_{m-\text{snow}} = 0.0597\, D^{-0.6}, \tag{29}$$

where the particle diameter D is in millimeters, and the resulting density is in grams per centimeter cubed. Graupel can collect snow, and snow can self-collect in this model. Two UW-NMS simulations are used in the current study. The first is a simulation of a thunderstorm complex observed during the Cooperative Huntsville Meteorological Experiment. Identified here as COHMEX, this simulation was performed on a 1-km, 51 × 51 grid domain. A description of COHMEX can be found in Mugnai et al. (1990). A second simulation was initialized with a balanced vortex and sounding data from the environment preceding the passage of Hurricane Gilbert (1988) at Kingston, Jamaica. The resulting hurricane simulation (hereinafter, HURRICANE) was performed on a two-way, multiply nested grid, which included a 3.3-km, 62 × 62 inner nest during the last 6 h of simulation time to resolve the inner core region of the storm. Details of HURRICANE may be found in Tripoli (1992b).

Depicted in Fig. 2 is a plan view of the surface rainfall-rate field in the TOGA1 tropical squall line simulation at 180 min into the simulation. On the right side of the figure is the bowed convective leading edge of the squall line with rain rates exceeding 16 mm h^{-1}. The leading-edge convection extends to the south and west (north is up in the figure). Less intense and more horizontally uniform stratiform precipitation trails the convection to the north and west.

The crossing of the dotted lines at $x = 42$ km and $y = 75$ km in Fig. 2 indicates the position of the test profile examined in this section. This grid point is located near the center of an area of stratiform rain, with a surface rainfall rate of 1.8 mm h^{-1}. The melting-layer model is applied to the TOGA1 simulation at the grid point. The top of the melting-layer model coincides with the 6-km level in the parent-model simulation, where the temperature is just below freezing (271.4 K), and the snow and graupel water contents are 0.17 and 0.25 g m^{-3}, respectively. The freezing level occurs 0.37 km below the melting-model top.

Presented in Figs. 3a,b are the water content and mass flux profiles, respectively, of snow, graupel, rain, and total precipitation calculated using the melting model. Note that to emphasize the melting-model physics, subsequent scaling of the precipitation mass flux using (23) is omitted in this example. From the top of the model domain to the freezing level, sublimation of ice reduces the mass and mass flux of both snow and graupel, and collection processes are weak (collection efficiency is less than 0.1). The melting of ice-phase particles falling below the freezing level is initially inhibited by the evaporation of meltwater [see (13)], a process that consumes most of the sensible heat flux to each particle while removing little mass. More-effective collection of snow by graupel and vice versa at these temperatures (collection efficiency of 1.0) causes a slight increase in the water content of snow while the water content of graupel decreases; however, the total mass flux of snow and graupel together is nearly constant from the freezing level to a depth of 0.75 km (about 0.4 km below the freezing level).

Below a depth of 0.75 km, the increasing humidity of the air effectively shuts off meltwater evaporation, and the increasing sensible heat flux from the air provides the latent heat required for rapid melting of snow and graupel (see Fig. 3e). The denser graupel particles require more time to melt than snow particles of the same size, and the graupel distribution is completely melted at a depth 0.25 km lower than snow. The melted and partially melted snow and graupel attain higher terminal velocities, and therefore the total water content of precipitation decreases rapidly with melting, despite the fact that the total mass flux of precipitation is nearly

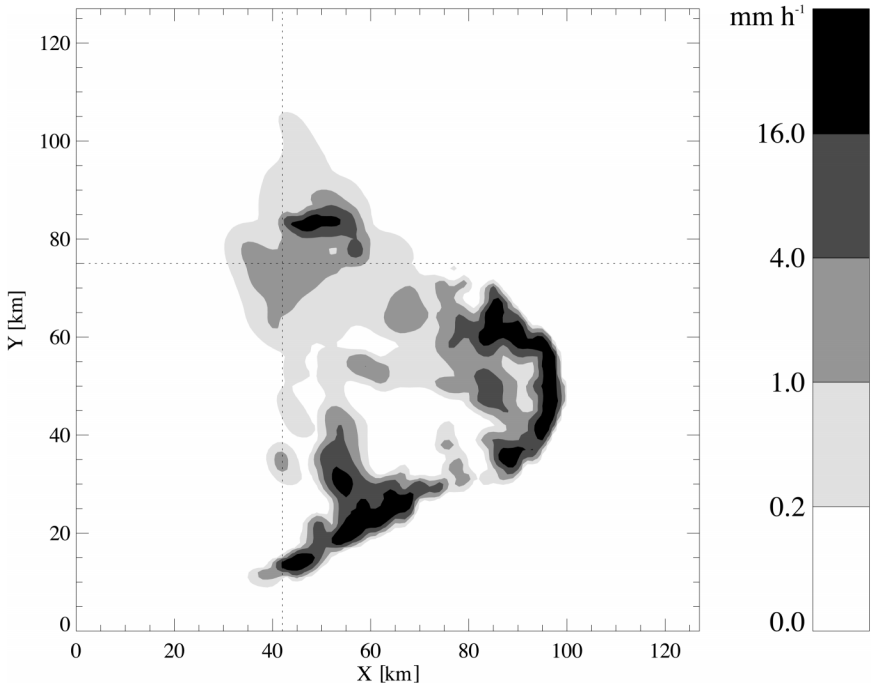

FIG. 2. Plan view of the surface rainfall rate distribution at 180 min from the TOGA1 CRM simulation. The location of the test profile is indicated by the crosshairs.

constant. At 1.8-km depth the snow and graupel are completely melted, and the gradual decrease of precipitation water content and mass flux below this level is caused by the evaporation of rain.

One of the limiting assumptions in the GCE model microphysics is that both snow and graupel particles have material densities independent of particle size. Studies by Locatelli and Hobbs (1974), Mitchell et al. (1990), and others suggest that the density of snow particles decreases markedly with size, but graupel particles show only a slight decrease in density with size. The snow density relationship of Mitchell et al. (1990) and a curve fit to the graupel observations of Locatelli and Hobbs (1974) yield

$$\rho_{m\text{-snow}} = 0.149D^{-1.0} \quad \text{and} \tag{30}$$

$$\rho_{m\text{-graupel}} = 0.144D^{-0.341}, \tag{31}$$

where D is in millimeters and $\rho_{m-\text{snow}}$ and $\rho_{m-\text{graupel}}$ are in grams per centimeter cubed. Note that the volume-weighted mean densities of snow and graupel are approximately 0.08 and 0.12 g cm^{-3}, respectively, according to (30) and (31). The mean density of graupel, in particular, is much lower than the prescribed graupel densities of 0.4 g cm^{-3} in the GCE model and 0.6 g cm^{-3} in the UW-NMS model. If graupel grows by collection of rimed snow, which is a primary mechanism in the 3D parent-model simulations of stratiform areas, then the lower mean density of graupel calculated using (31) may be more appropriate for melting-layer simulations.

Snow and graupel with the density distributions in (30) and (31) are substituted for the snow and graupel distributions at 6 km at the same grid point of the TOGA1 simulation, and the number densities of both types of particles are scaled to yield the same water contents as those in the original simulation. The modified snow and graupel distributions are then used to initialize the melting model, with the resulting profiles of precipitation water contents and mass fluxes shown in Figs. 3c and 3d, respectively.

In comparing the model profiles to the profiles based upon the fixed-density particles in Figs. 3a,b, it may be noted that the primary difference is the more rapid melting of the variable-density particles. The depth of the melting layer contracts from about 1.0 km to 0.5 km. This result is due to the fact that the larger snow and graupel particles, which are less dense than their constant-density counterparts, melt completely in a shorter period of time. These larger particles require the most time to melt and therefore constrain the melting time of the entire distribution. The differences in particle density have an impact on the radiative properties of the melting band to be discussed in section 2d.

c. *Dielectric properties of melting hydrometeors*

1) MAXWELL-GARNETT MODEL

Generally, the effective dielectric constant of an inhomogeneous particle is calculated as a function of the individual contributions by ice, liquid water, and air.

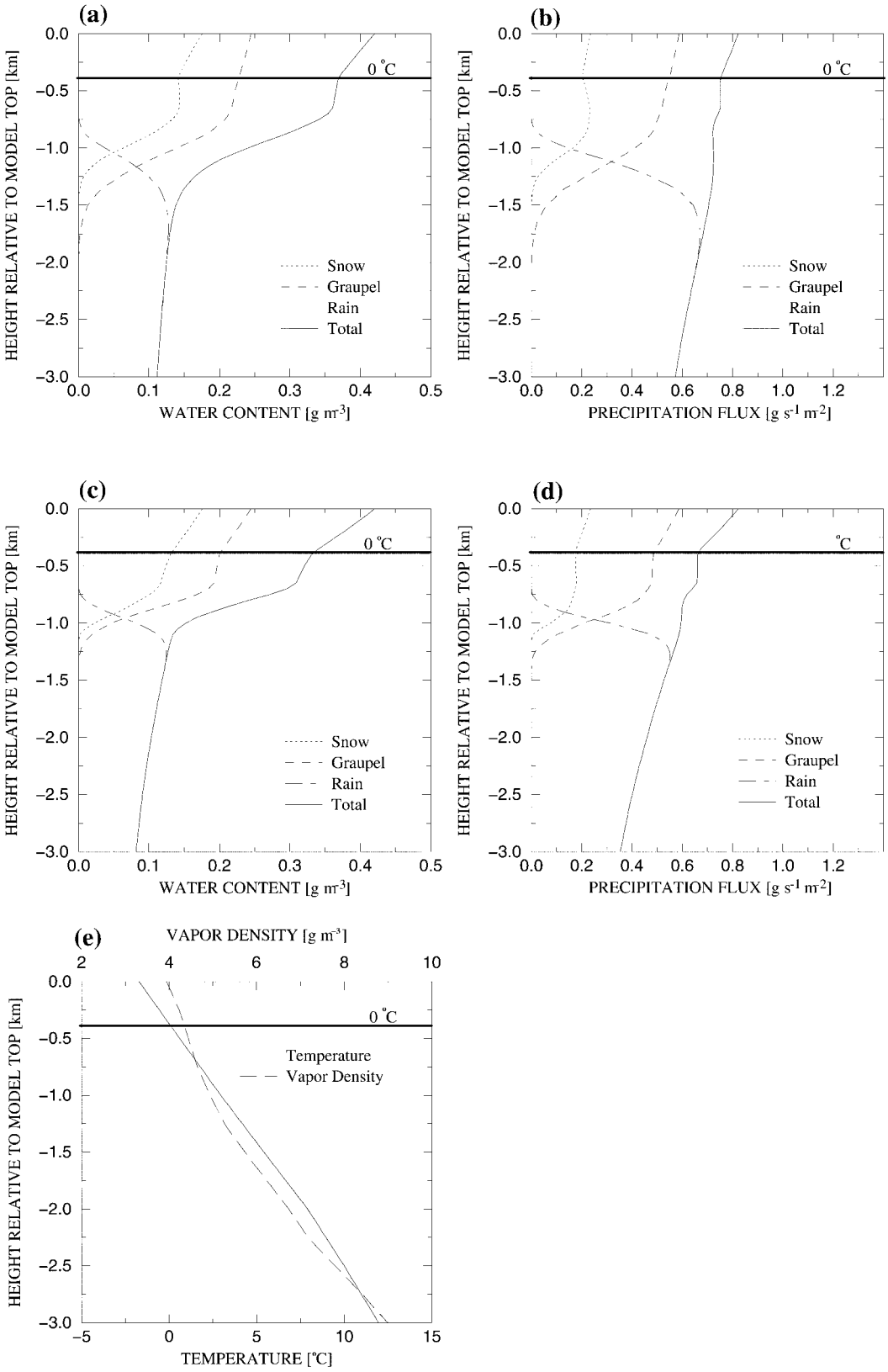

FIG. 3. Melting-layer model vertical profiles of (a) precipitation water contents and (b) precipitation mass fluxes based upon melting of snow and graupel with size-independent densities. (c), (d) The same as (a) and (b), but for snow and graupel densities that decrease with size. (e) Temperature and water vapor density profiles.

The most widely used formulation follows the Maxwell-Garnett approach (Maxwell-Garnett 1904) which was generalized by Bohren and Battan (1982). An inhomogeneous particle is described as a matrix material with randomly distributed and oriented elliptical inclusions that contribute to the effective dielectric constant of the particle in proportion to their volume fraction, f_{inc}:

$$\varepsilon_{\text{mix}} = \frac{(1 - f_{\text{inc}})\varepsilon_{\text{mat}} + f_{\text{inc}}\zeta\varepsilon_{\text{inc}}}{1 - f_{\text{inc}} + f_{\text{inc}}\zeta}, \tag{32}$$

where

$$\zeta = \left(\frac{2\varepsilon_{\text{mat}}}{\varepsilon_{\text{inc}} - \varepsilon_{\text{mat}}}\right)\left[\left(\frac{\varepsilon_{\text{inc}}}{\varepsilon_{\text{inc}} - \varepsilon_{\text{mat}}}\right)\ln\left(\frac{\varepsilon_{\text{inc}}}{\varepsilon_{\text{mat}}}\right) - 1\right]. \tag{33}$$

Here, ε_{mat}, ε_{inc}, and ε_{mix} denote the complex dielectric constant of the matrix, the inclusions, and the mixture, respectively, and $\ln(\varepsilon_{\text{inc}}/\varepsilon_{\text{mat}})$ is the principal value of the complex number $\varepsilon_{\text{inc}}/\varepsilon_{\text{mat}}$. For three component mixtures, (32) must be applied twice, and the resulting dielectric constant of the mixture depends upon the order of application as well as the choice of matrix and inclusion materials in each application.

2) MENEGHINI AND LIAO MODELS

Meneghini and Liao (1996, hereinafter ML96) solved the electromagnetic field equations numerically for particles subdivided into a grid of cells containing ice, air, or liquid water. The effective dielectric constants of the particles were then determined as those which, when input to Mie theory, produced the same extinction and backscatter coefficients as the numerical technique. For a spatially homogeneous ice–water mixture, that is, meltwater pockets randomly distributed throughout the particle volume, these authors developed an analytical function to better represent the particle dielectric constant $\varepsilon_{\text{ML96}}$ at a frequency of 7.7 GHz. At intermediate melting stages they utilized an error function to interpolate between the dielectric constant of an ice matrix with liquid water inclusions $\varepsilon_{\text{MGiw}}$ (MGiw, initial melting stage) and that of a water matrix with ice inclusions $\varepsilon_{\text{MGwi}}$ (MGwi, later melting stage), as a function of the fractional volume of ice f_{ice}. In this study, $f_{\text{ice}} + f_{\text{air}}$ is substituted for f_{ice}, and the Maxwell-Garnett formula for air inclusions in an ice matrix is used to compute the dielectric constant of the ice–air mixture.

More recently, Meneghini and Liao (2000, hereinafter ML00) improved the numerical accuracy of their dielectric constant calculations, employing a continuous, multiple-component particle approach with parameterizations which allowed for applications to frequencies between 10 and 95 GHz. Their dielectric constant model $\varepsilon_{\text{ML00}}$ was based upon the assumption that the properties of the particle constituents are homogeneous, isotropic, and linearly superimposed. For a particle consisting of a mixture of ice, air, and liquid water, an analytical approximation for $\varepsilon_{\text{ML00}}$ was developed using Debye theory to compute the particle air–ice electric field ratios and by fitting the numerically derived water–ice electric field ratios to linear functions of water fraction. A small bias in the dielectric constant is introduced by these approximations.

3) FABRY–SZYRMER CORE-SHELL MODEL

For the purpose of modeling radar reflectivities in the melting layer, Fabry and Szyrmer (1999, hereinafter FS) represented melting snow particles using a concentric core and shell with different dielectric properties. In their model, the particle core consists of ice inclusions in a liquid water matrix, which together serve as a matrix for air inclusions. The latter are treated as bubbles in a comparatively solid environment. The outer shell is modeled as ice inclusions in a water matrix, which together form inclusions in a matrix of air. Thus the outer shell represents a tenuous collection of melting ice crystals. The dielectric constants of the core and shell are calculated using (32). As the particle melts, the core and shell densities approach 1.0 g cm^{-3} (completely melted), and the core radius fraction α also approaches 1 (the melted particle radius).

If the core region of the particle is treated as a spherical inclusion within a matrix of shell material, the effective dielectric constant of the complete particle can be approximated by the original Maxwell-Garnett theory. Under this assumption, the effective dielectric constant is

$$\varepsilon_{\text{FS}} = \varepsilon_{\text{shell}} + \frac{3\varepsilon_{\text{shell}}\alpha^3(\varepsilon_{\text{core}} - \varepsilon_{\text{shell}})}{\varepsilon_{\text{core}} + 2\varepsilon_{\text{shell}} - \alpha^3(\varepsilon_{\text{core}} - \varepsilon_{\text{shell}})}, \tag{34}$$

where $\varepsilon_{\text{core}}$ and $\varepsilon_{\text{shell}}$ are the permittivities of the core and shell regions, respectively. However, (34) is only appropriate if the particle dimensions are small as compared with the wavelength of radiation, a condition that is not always satisfied in the current applications. Thus, for the purpose of calculating particle radiative properties, the rigorous solution of the electromagnetic field equations applied to a core-shell system will be utilized, as in FS (see section 2d).

4) INTERCOMPARISON OF DIELECTRIC CONSTANT MODELS

Particle dielectric constants at 10.65, 19.35, 37.0, and 85.5 GHz are calculated for melting snow (initial ρ_m = 0.1 g cm^{-3}) and graupel (initial ρ_m = 0.4 g cm^{-3}) and converted to refractive indices using

$$n = \sqrt{\varepsilon}. \tag{35}$$

Melting snow and graupel refractive indices are presented in Figs. 4 and 5, respectively. The five curves in each panel correspond to calculations using the different dielectric models described in the previous subsections. The curves converge to points near the lower

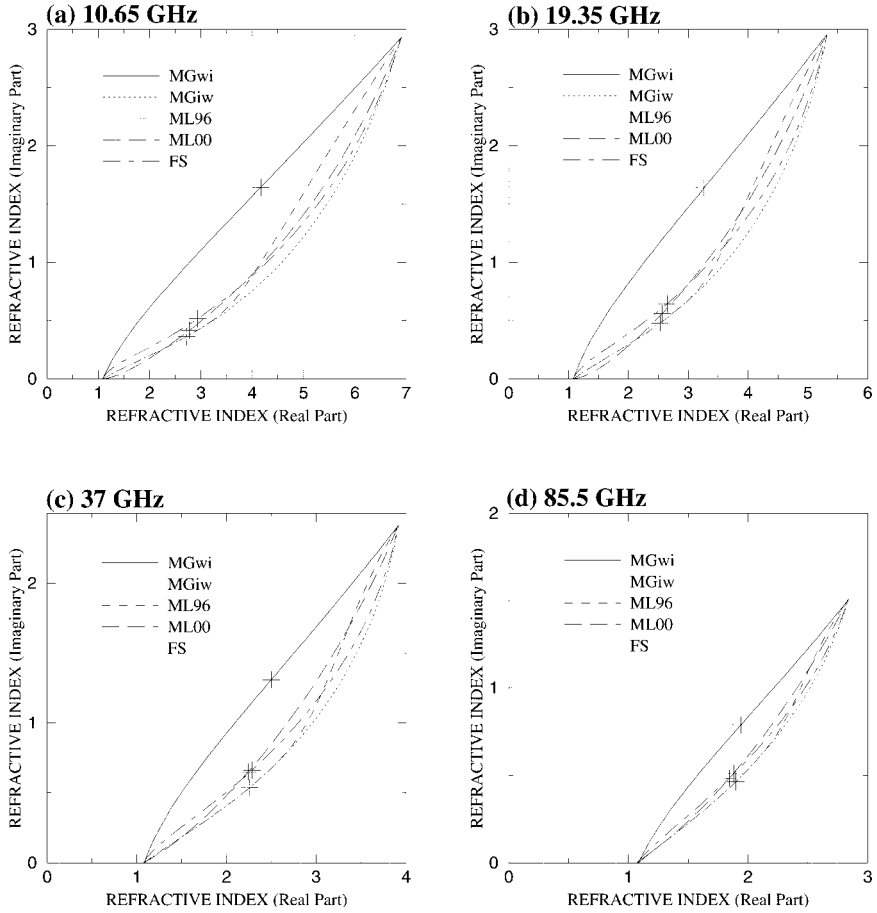

FIG. 4. The real and imaginary parts of the refractive indices of melting snow based upon different dielectric constant models at (a) 10.65, (b) 19.35, (c) 37, and (d) 85.5 GHz. The lower-left vertex of the model curves in each panel represents dry snow; the upper-right vertex represents completely melted snow. The "+" on each model curve represents a melted particle fraction of 0.5 by volume.

left (no meltwater) and upper right (completely melted) corners of each panel, with a "+" indicating a meltwater volume fraction of 0.5.

It may be noted from the figures that the refractive index curves are generally bounded by the MGwi and MGiw model curves. The quasi-linear MGwi curve yields the maximum rate of increase of the imaginary component of refractive index with melting. Conversely, the MGiw model typically yields the smallest rate of increase of the imaginary component. The other three models tend to follow the behavior of MGiw but with noted differences. ML96 closely follows MGiw up to a volume meltwater fraction of 0.5, but then it makes a transition to MGwi for higher meltwater fractions. The ML00 model yields imaginary refractive indices sometimes lower than those produced by MGiw for very low meltwater fractions, but then gradually diverges from the MGiw curve for higher meltwater fractions. In contrast, the FS model yields a higher imaginary refractive index component than either ML96 or ML00 for meltwater fractions less than 0.5, but then approaches the MGiw model refractive index as the meltwater fraction increases from 0.5 to 1.0.

The refractive indices of snow and graupel are subtly different. A close inspection of Figs. 4 and 5 reveals greater real and imaginary refractive index components for graupel with a given meltwater fraction for all but the MGwi model. The MGwi model yields slightly smaller refractive indices for graupel relative to snow. Overall, the refractive index differences between snow and graupel decrease as the meltwater fraction increases.

d. Radiative properties

Plotted in Fig. 6 are the absorption and scattering efficiencies of FS snow particles at 10.65, 19.35, 37.0, and 85.5 GHz. The efficiencies are calculated based upon the analytical solution for electromagnetic waves interacting with a dielectric sphere having a core and outer shell (see Bohren and Huffman 1983). The absorption and scattering efficiencies, multiplied by a particle's geometric cross section, are proportional to the

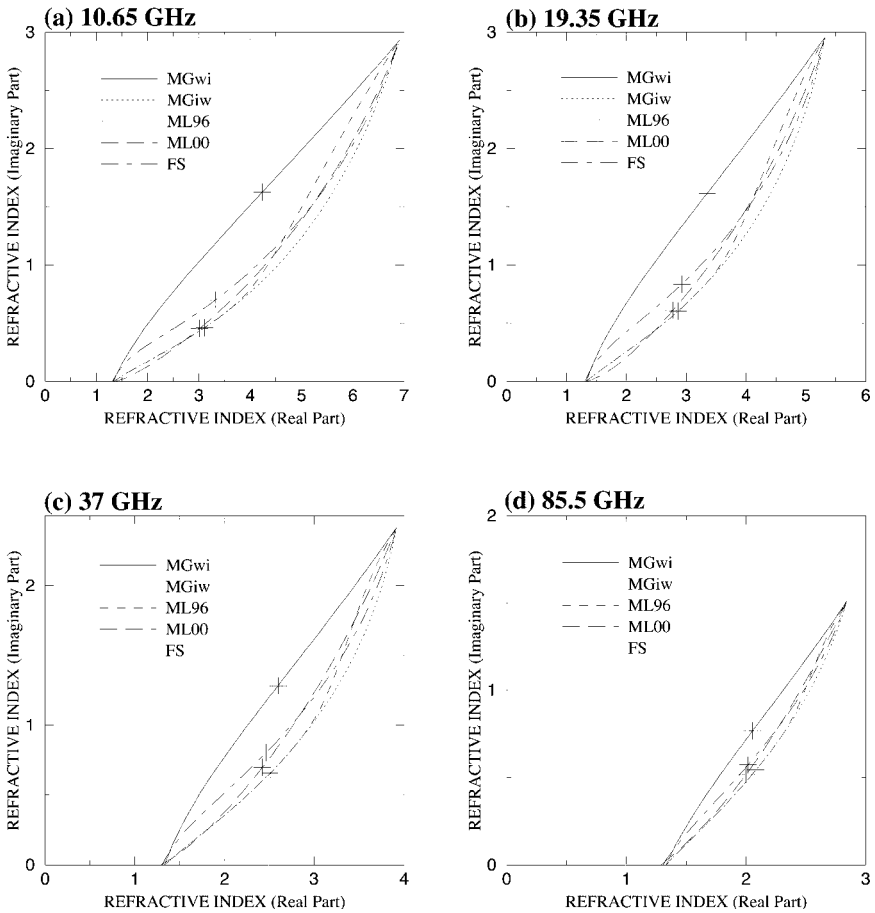

FIG. 5. Same as Fig. 4, but for melting graupel.

radiative power absorbed and scattered by the particle at these TMI channel frequencies. Presented in each plot are efficiency curves for five different meltwater volume fractions spanning the range from ''dry'' snow (ρ_m = 0.10 g cm^{-3}) to pure liquid composition. At all frequencies and for all particle compositions, the efficiencies increase with increasing particle size until the particle radius is approximately one-tenth the wavelength of radiation. At larger particle radii, maximum efficiencies are first attained by the pure liquid particles, and then successively by particles with decreasing meltwater fractions. Dry snow particles have very low absorption and scattering efficiencies, with the exception of relatively large particles at 37.0 and 85.5 GHz.

For relatively small volume fractions of meltwater (less than ~0.10), absorption and scattering efficiencies of the particles generally increase with meltwater fraction. The increase of efficiency with meltwater fraction is greatest for the smallest meltwater fractions, a nonlinear sensitivity that has been noted by other investigators (e.g., Meneghini and Liao 1996). Considering particles with radii greater than about one-tenth the wavelength of radiation, note that the absorption efficiencies are maximized for intermediate meltwater fractions (~0.4), whereas the efficiencies of pure liquid drops of the same size are less. The same trend is not seen in particle scattering efficiencies, which nearly always increase with increasing meltwater fraction. The implication of these trends is that the radiometric absorption/emission and scattering by only slightly melted particles can be significant when compared with pure liquid drops of the same size and that the absorption/emission by particles with significant melted fractions can actually exceed that of pure liquid drops.

The individual particle properties are integrated over the size distribution of each particle species in the test profiles depicted in Fig. 3a to produce the profiles of bulk absorption and scattering coefficients in Figs. 7a and 7b, respectively. These bulk absorption and scattering coefficients are based upon application of the FS dielectric model to both snow and graupel. For comparison, absorption and scattering coefficients based upon the MGwi model are plotted in Figs. 7c and 7d, respectively.

It may be inferred from Fig. 7a that the bulk absorption by melting snow and graupel is greater than the absorption by rain alone at the base of the melting layer. The higher water contents of precipitation (Fig. 3a) as

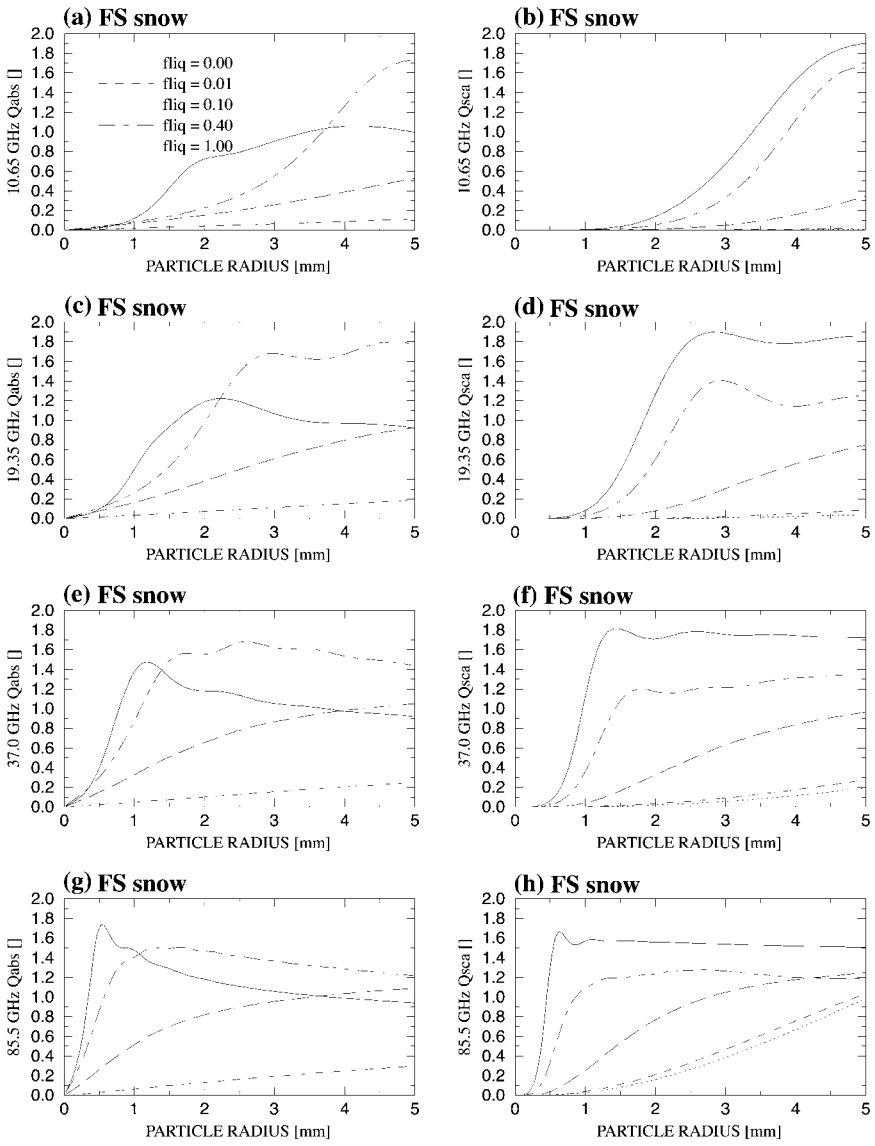

FIG. 6. Absorption and scattering efficiencies at (a), (b) 10.65, (c), (d) 19.35, (e), (f) 37.0, and (g), (h) 85.5 GHz, plotted as functions of particle radius based upon the FS dielectric constant model for snow particles with meltwater volume fractions of 0.0, 0.01, 0.1, 0.4, and 1.0.

well as the elevated absorption efficiencies of partially melted precipitation (Figs. 6a,c,e,g) contribute to greater absorption in the melting layer. Maximum absorption occurs about 0.5 km below the freezing level based upon the FS model, and it is about an order of magnitude greater than the absorption by rain below the melting layer at 10.65 GHz. Maximum absorption is about 5, 3, and 2 times the absorption by rain at 19.35, 37.0, and 85.5 GHz, respectively. Microwave scattering is also maximized in the melting layer. However, at frequencies less than 85.5 GHz, scattering is generally much less than absorption, and the scattering peaks are broader, extending through the depth of the melting layer (Fig. 7b). The broader scattering peaks result from the less rapid, monotonic increase of scattering efficiency with melted particle fraction, as seen in Figs. 6b,d,f,h, whereas the absorption efficiency increases more rapidly with melted fraction for a wide range of particle sizes (Figs. 6a,c,e,g). At 85.5 GHz, absorption and scattering in the melting layer are comparable. The absorption and scattering coefficients based upon the MGwi model exhibit similar trends, with slightly higher peaks of absorption and scattering given by MGwi.

In Fig. 8, the extinction efficiency and normalized backscatter cross section based upon the FS model are plotted for snow particles with various volume fractions of meltwater at 13.8 GHz, the operating frequency of the PR. The extinction efficiency, multiplied by the particle's geometric cross section, is proportional to the radar attenuation by the particle. Similarly, the nor-

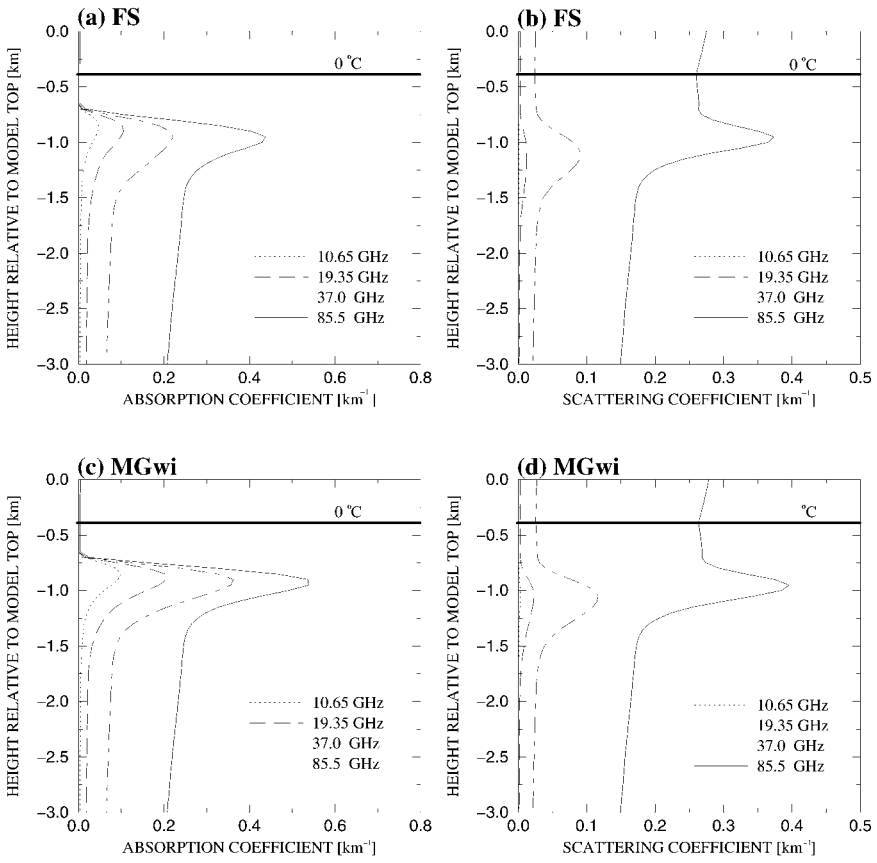

FIG. 7. Melting-layer vertical profiles of (a) absorption coefficient and (b) scattering coefficient at 10.65, 19.35, 37.0, and 85.5 GHz, based upon the FS dielectric constant model applied to the snow and graupel distributions plotted in Fig. 3a. (c), (d) Absorption coefficient and scattering coefficient profiles based upon the MGwi dielectric constant model.

malized backscatter cross section multiplied by the particle geometric cross section is proportional to the radar power reflected by the particle. The extinction efficiencies at 13.8 GHz (Fig. 8a) follow the same trends as the absorption efficiencies at 10.65 GHz (Fig. 6a). It may be inferred that radar attenuation becomes significant with the onset of particle melting. On the other hand, for a particle of fixed size, the backscatter cross section increases almost in proportion to the liquid water fraction.

The individual particle extinction efficiencies and backscatter cross sections are integrated over the size distribution of each particle species in the test profiles depicted in Fig. 3a to produce the profiles of bulk extinction coefficient and radar reflectivity in Figs. 9a and 9b, respectively. These profiles are based upon the FS dielectric model, and the contributions from snow, graupel, and rain are indicated. For comparison, extinction coefficients and radar reflectivities based upon the MGwi model are plotted in Figs. 9c and 9d, respectively.

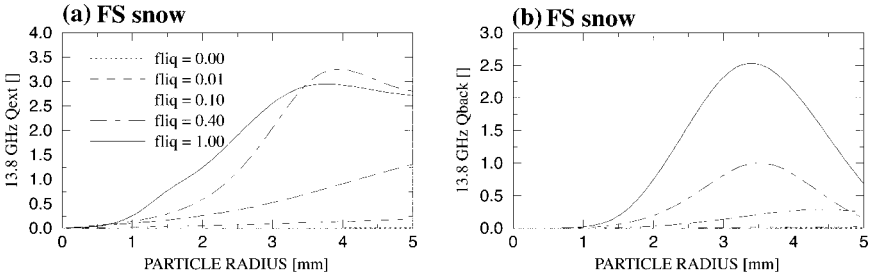

FIG. 8. (a) Extinction and (b) backscatter efficiencies at 13.8 GHz, plotted as functions of particle radius based upon the FS dielectric constant model for snow particles with meltwater volume fractions of 0.0, 0.01, 0.1, 0.4, and 1.0.

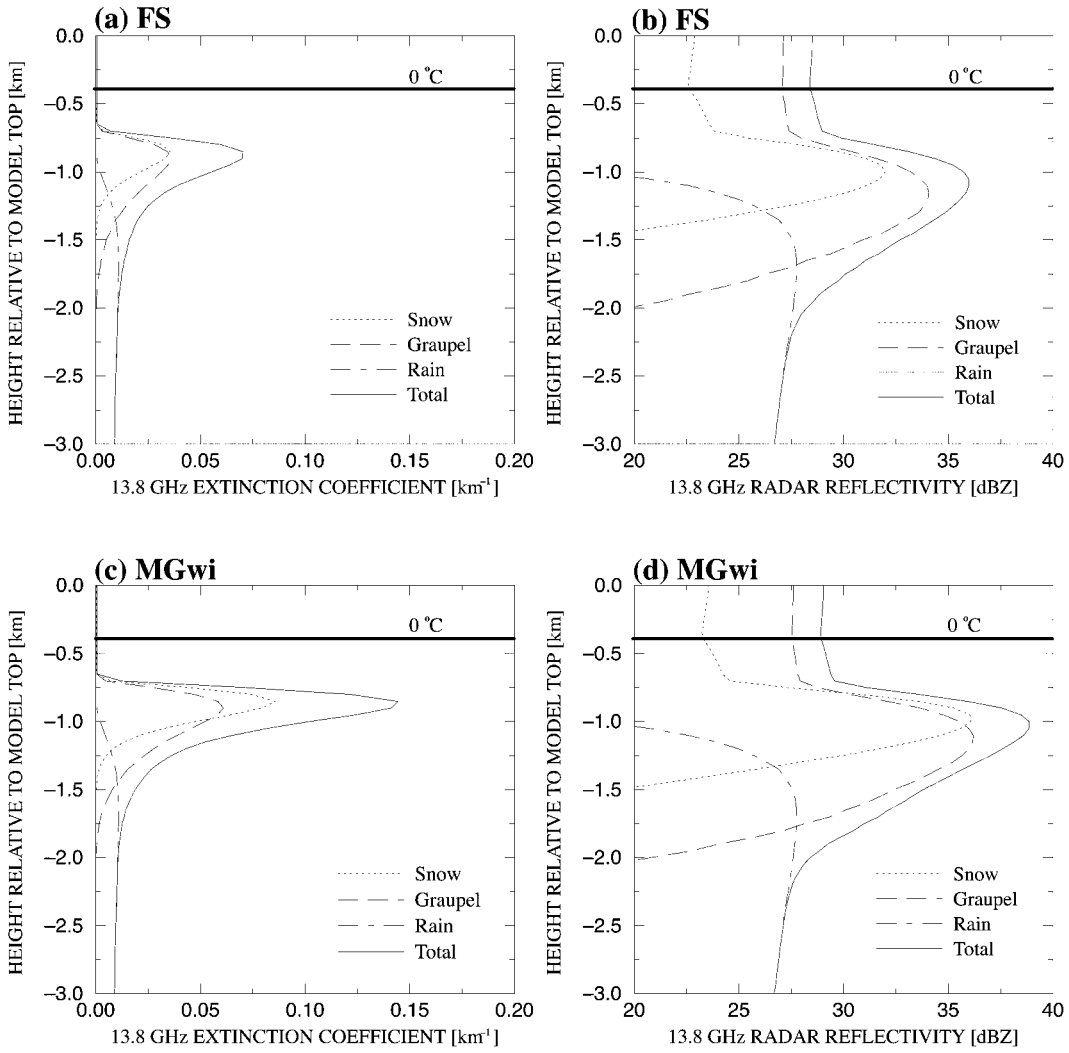

FIG. 9. Melting-layer vertical profiles of (a) extinction and (b) reflectivity at 13.8 GHz, based upon the FS dielectric constant model applied to the snow and graupel distributions plotted in Fig. 3a. (c), (d) Extinction and reflectivity profiles based upon the MGwi dielectric constant model.

Because microwave scattering is almost negligible in comparison with absorption at 13.8 GHz, the profiles of total extinction have almost the same form as the profiles of absorption shown in Fig. 7a. Note that the peak extinction by snow is almost the same as that of graupel, even though the water content of graupel is always greater than that of snow (Fig. 3a). This result is explained by the greater proportion of large particles, which have greater extinction efficiencies, in the snow distribution according to the GCE model microphysics. The greater proportion of large snow particles offsets the slightly greater extinction efficiency of graupel. On the other hand, because of their lower density, snow particles completely melt in a shorter period of time than do graupel particles of the same size, leading to a relatively narrow peak of snow extinction. The peak reflectivity of the melting band reaches nearly 37 dBZ about 0.6 km below the freezing level, where the slower-melting graupel makes a greater contribution to the reflectivity. The peak reflectivity of the melting layer greatly exceeds the reflectivity of rain below the melting layer (~27 dBZ). Note also that the peak of reflectivity is at a slightly lower altitude than the peak of extinction. This effect is explained by the more gradual increase of backscatter efficiency (relative to extinction efficiency) with meltwater fraction (see Fig. 8). The greater refractive indices produced by the MGwi model for melting particles lead to generally greater extinction and reflectivity in the melting layer (Figs. 9c,d).

Snow and graupel with initial densities that decrease with size according to (30) and (31), respectively, also have lower mean densities. These ice distributions completely melt within a thinner layer (Figs. 3c,d). Radiative extinction is reduced roughly in proportion to the reduced water contents of the mixed-phase particles (Fig. 10a). Reflectivity is controlled by the larger, less dense

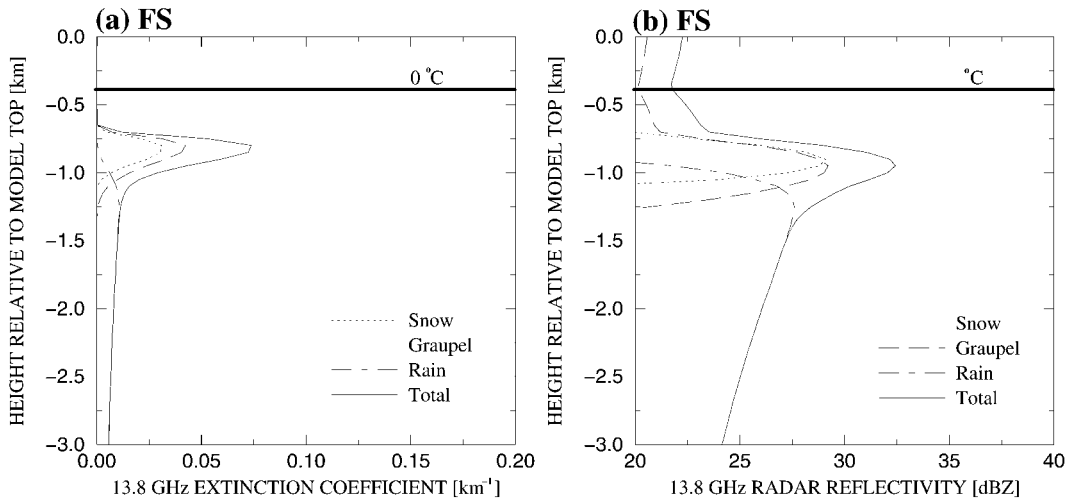

FIG. 10. Melting-layer vertical profiles of (a) extinction and (b) reflectivity at 13.8 GHz, based upon the FS dielectric constant model applied to the snow and graupel distributions plotted in Fig. 3c.

particles, and the sizes of these particles are more quickly reduced in the process of melting, resulting in substantially lower reflectivities in the melting layer (Fig. 10b).

3. Comparison of melting-band simulated attenuation with radar observations

The aspect of the melting band model that is, perhaps, most relevant to radiometer and radar remote sensing of precipitation is whether the model can simulate the extinction of microwave radiances. In the previous section it was demonstrated that radiative absorption and scattering per kilometer within the melting layer could be several times the absorption and scattering per kilometer of the fully melted precipitation below. This absorption and scattering could have an impact on the upwelling radiances measured by passive microwave radiometers. In a similar way, the additional extinction in the melting layer could lead to greater attenuation of reflectivities below the layer, as observed by spaceborne radar.

Here, the radar ''mirror-image'' technique (see Liao et al. 1999) is applied to observations of the PR in stratiform rain areas to estimate the radiative extinction associated with melting precipitation. A schematic of a PR reflectivity profile is provided in Fig. 11 for the identification of specific reflectivity measurements described in the analysis. Mirror-image reflectivities refer to reflectivities measured at ranges beyond the range of the surface reflection. These reflectivities are produced by radar pulses that have reflected off the earth's surface, are then backscattered by a precipitation target, and are finally reflected off the earth's surface a second time toward the radar receiver. The current application of the technique to PR observations follows.

First, nadir-view reflectivity profiles and derived products from the PR are collected from the period of 4–22 August 1998, over the region bounded by 20°S and 20°N latitude, 180° and 120°W longitude. The data are filtered using the qualitative flags in the derived TRMM product 2A23 (Awaka et al. 1998) to select only profiles in which stratiform rain was present and a radar

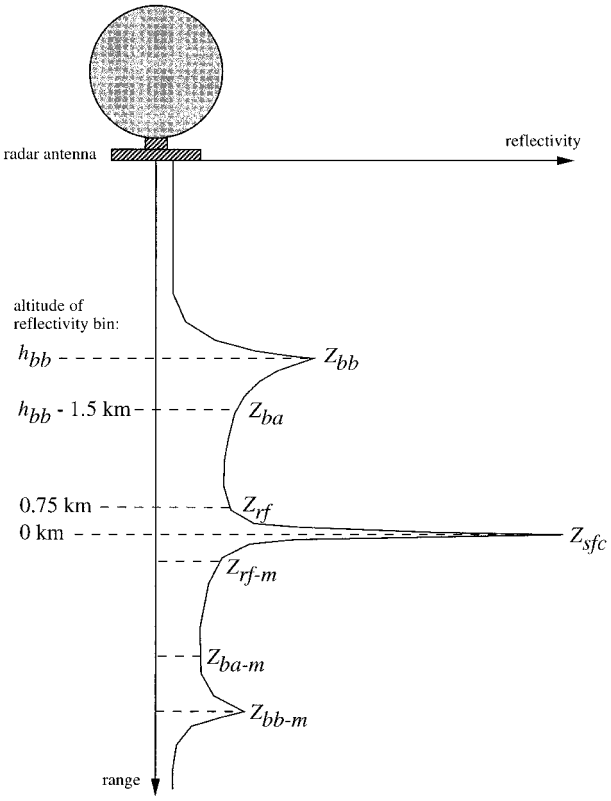

FIG. 11. Schematic of reference levels utilized to determine melting-layer extinction optical depths from PR measurements.

bright band was detectable. The reflectivities of each three consecutive nadir profiles are averaged to reduce noise for subsequent processing. The averaged profiles are next analyzed to identify the brightband reflectivity bin (maximum reflectivity bin within 1.5 km of the maximum reflectivity gradient above the rain layer). The range difference between the radar surface return and the bright band is calculated, and then the brightband mirror-image bin is identified as the maximum reflectivity bin within 0.75 km of an equal range displacement beyond the surface return. If either the brightband reflectivity Z_{bb} or the reflectivity of its mirror image Z_{bb-m} is below 25 dBZ, the profile is rejected. An alternate surface range is defined as the average of the brightband range and the brightband mirror-image range. If this surface range deviates by more than 0.125 (one-half a range bin) from the range of the maximum surface return, then the profile is rejected. A ''basal'' reflectivity Z_{ba} and a ''basal-mirror'' reflectivity Z_{ba-m} are then identified as those corresponding to bins 1.5 km below the bright band and its mirror image, respectively. Also, a ''reference'' reflectivity Z_{rf} and a ''reference-mirror'' reflectivity Z_{rf-m} correspond to bins 0.75 km above and below the surface return. If any of the reflectivities of the basal, basal-mirror, reference, or reference-mirror are less than 20 dBZ, the profile is rejected. The purpose of the filtering process is to remove profiles that 1) do not have an easily identifiable bright band or brightband mirror image, 2) have uncertain brightband or mirror-image brightband ranges relative to the surface range, and 3) do not have basal, basal-mirror, reference, and reference-mirror reflectivities that are significantly greater than the minimum-detectable limit ($\sim$17 dBZ).

Profiles that survive the filtering process are analyzed to estimate the optical depth between the brightband height and the level 1.5 km below the bright band. Although it may be argued that the bulk of the extinction due to melting, based upon Figs. 9 and 10, lies between the top of the bright band and a kilometer below the top, application of the mirror-image technique requires well-defined reference levels and reflectivity measurements that are relatively noise insensitive. Radar reflectivities above the brightband maximum are often close to the minimum-detectable limit, and the brightband maximum and its mirror image supply well-defined height references. A 1.5-km layer depth ensures that the melting process is entirely contained within the layer and puts the base reflectivity and its mirror image below the gradient region associated with melting, establishing a more certain reflectivity reference.

Following the method of Liao et al. (1999), reflectivity double differences are defined by

$$\Omega_{bb} = (Z_{bb} - Z_{bb\text{-}m}) - (Z_{rf} - Z_{rf\text{-}m}), \quad \text{and} \tag{36}$$

$$\Omega_{ba} = (Z_{ba} - Z_{ba\text{-}m}) - (Z_{rf} - Z_{rf\text{-}m}) \tag{37}$$

(all reflectivities: dBZ). For ideal, beam-filling radar targets and specular reflection of the nadir-view radar beam off a flat ocean surface, the measured difference Ω_{bb} would be 4 times the radar path attenuation (four-way attenuation) between the bright band and the 0.75-km-altitude reference level. In a similar way, Ω_{ba} would be the four-way attenuation between the basal level and the reference level. For wind-roughened ocean surfaces, Liao et al. (1999) modeled the four-way attenuation between any altitude h and the surface. Their four-way attenuation simulations were fit to an empirical function, $\Gamma(\Omega, h, \sigma^o)$, where Ω is the PR-measured double difference between h and 0.75-km altitude, and σ^o is the surface radar backscatter cross section. Using this function, measurements of Ω_{bb} and Ω_{ba}, and an estimate of the surface backscatter cross section σ^o from nadir-view PR measurements in rain-free regions (TRMM 2A21 product; Meneghini et al. 2000), the optical depth τ between the bright band and the basal level can be estimated from

$$\tau = \frac{\ln(10)}{40}[\Gamma(\Omega_{bb}, h_{bb}, \sigma^o) - \Gamma(\Omega_{ba}, h_{bb} - 1.5 \text{ km}, \sigma^o)], \tag{38}$$

where h_{bb} is the altitude of the bright band.

Equation (38) is applied to the filtered PR reflectivity profile data from August of 1998 and the resulting estimates of τ are plotted versus corrected basal reflectivity measurements Z^*_{ba} in Fig. 12. The basal reflectivities are corrected using

$$Z^*_{ba} = Z_{ba} + \frac{20}{\ln(10)}\tau, \tag{39}$$

(reflectivities: dBZ). The correction [(39)] compensates for the attenuation of the basal reflectivity due to overlying precipitation between the basal level and the bright band. This correction makes Z^*_{ba} a parameter representative of the ''output'' precipitation below the melting layer, which is more or less independent of optical depth variations in the precipitation above. In this way, the impact of optical depth variations in the melting layer is seen primarily along the optical depth axis of the plots in Fig. 12. Error bars are calculated based upon the estimated uncertainties in the PR reflectivity data, the altitudes of the brightband and basal-reflectivity bins, and the surface backscatter cross section. Because the error bars do not vary greatly over the distribution of plotted values, they are plotted for only one representative point in each panel.

Also plotted in the different panels of Fig. 12 are the optical depths corresponding to corrected basal reflectivities calculated using the melting-layer model developed in this study. The melting model profiles are initialized using the snow and graupel water contents just above the freezing level in stratiform areas of the TOGA1 and TOGA3 model simulations. Four variations of the melting-layer simulations are represented in the figure. The first is a melting simulation in which partially melted ice hydrometeors are ''refrozen,'' such that

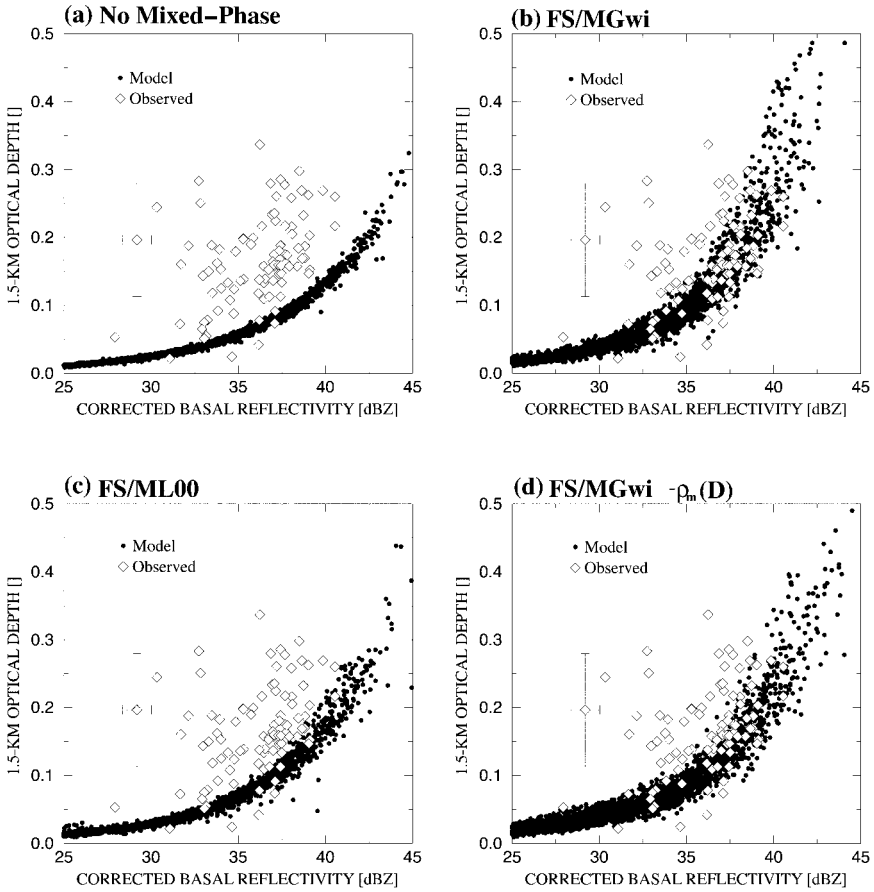

FIG. 12. Extinction optical depths of simulated melting layers (black dots), plotted as functions of attenuation-corrected basal reflectivities using (a) no mixed-phase particles, (b) FS model snow and MGwi model graupel, (c) FS model snow and ML00 model graupel, and (d) FS model snow and MGwi model graupel (but for snow and graupel densities that decrease with particle size). Melting layers are derived from the TOGA1 and TOGA3 cloud-resolving model simulations; see Table 1. Also, observed melting-layer extinction optical depths (diamonds) are plotted as functions of attenuation-corrected basal reflectivities. Observed optical depths are estimated using the mirror-image technique, applied to PR observations at low latitudes. Representative error bars are indicated for one pair of observations.

the meltwater is converted to an ice–air mixture with the same material density as the remainder of the frozen particle. Only when a snow or graupel particle is completely melted is it converted to pure liquid (raindrop). This first simulation therefore represents a control in which the dielectric properties of mixed-phase, partially melted ice particles are not considered. In a second melting simulation, the dielectric properties of snow are described using the FS model, and graupel dielectric properties are described using the MGwi model. A third melting simulation again incorporates the FS model for snow but substitutes the ML00 model for graupel. A fourth simulation incorporates the FS and MGwi models for snow and graupel, respectively, but alters the density distributions of snow and graupel according to (30) and (31).

Even considering the uncertainties in the PR-observed optical depths, Fig. 12 indicates a significant range of melting-layer optical depths corresponding to corrected basal reflectivities between 25 and 40 dBZ. Optical depths between 0.025 and 0.35 are derived from the mirror-image technique, and there is a trend of higher optical depths with higher basal reflectivities. In contrast, the melting model containing no mixed-phase particles (Fig. 12a) produces systematically lower optical depths for a given basal reflectivity. This systematic difference can be partly explained by the uncertainty in the observed optical depths and natural variations in precipitation particle size distributions that are not represented in the melting model. Because the current melting model does not include a description of the evolution of the raindrop size spectrum, the issue of varying particle distributions cannot be fully addressed here.

The presence of mixed-phase, melting ice hydrometeors can at least partly explain the observed optical depth distribution. Plotted in Fig. 12b are the optical

depth-corrected basal reflectivity pairs from the melting-model simulation based upon the FS model for snow and the MGwi model for graupel. Note that there is a much greater breadth of optical depths produced by this simulation and a much greater overlap with the distribution of observed optical depths in comparison with the simulation without mixed-phase particles. The greater overlap of the distributions is the result of two effects: first, there is a general increase in the optical depths of the simulated melting layers that is due to absorption by mixed-phase particles; second, the corrected basal reflectivities are slightly lower because of greater attenuation by precipitation above the bright band. Still, in the observed distribution at lower basal reflectivities there are a few relatively high melting-layer optical depths that are not explained by the FS–MGwi simulation.

If the ML00 model is substituted for MGwi to describe the dielectric properties of graupel (Fig. 12c), somewhat lower optical depths result, but these are still generally higher than those produced by the model with no mixed-phase particles. Even though ML00 provides a fairly rigorous description of homogeneous melting particles, the radiative extinction produced by these particles may be insufficient to explain the observed optical depths. Snow and graupel particles with empirical size-dependent densities are substituted for the constant-density particles from the GCE parent simulations to obtain the modeled optical depths and basal reflectivities of Fig. 12d. Note that the modeled optical depths have a greater spread than those produced by the constant-density particles at basal reflectivities less than about 33 dB*Z*, and they are generally lower than those produced by the constant-density particles at higher basal reflectivities. A simple explanation of these distributions is difficult, because the variable-density particles generally produce shallower melting layers with smaller optical depths, but, at the same time, corrected basal reflectivities are also reduced (Figs. 9a,b vs Figs. 10a,b). Overall, the optical depth distributions from the constant- and variable-density particles are very similar.

Although the foregoing analysis does not confirm the validity of any particular melting-model simulation, it does suggest that greater consistency between observed and simulated radiative properties of the melting layer can be achieved when the dielectric properties of mixed-phase, partially melted precipitation particles are included in the simulations. Moreover, the FS dielectric model for snow, combined with the MGwi dielectric model for graupel, produces the greatest overlap between the observed and simulated optical depth/reflectivity distributions. The observed distribution of melting-layer optical depths includes some relatively large values that are not simulated by any of the melting models. These large optical depths may be due to uncertainties in the observations; however, they may simply be unexplained because of a lack of realism/generality in the melting simulations. The simulations are subject to errors in the dielectric modeling of melting particles and inaccuracies in the prescribed precipitation particle size and density distributions, and these uncertainties could lead to model statistical properties that deviate from those observed.

4. Summary and outlook

In this study, a 1D steady-state microphysical model that describes the vertical distribution of melting precipitation particles is developed. The model is driven by the ice-phase particle (snow, graupel) distributions just above the freezing level at applicable horizontal grid points of parent 3D CRM simulations and extends these simulations by calculating the number density and meltwater fraction of each particle in finely separated size categories through the melting layer. The depth of the modeled melting layer is primarily determined by the initial material density of ice-phase particles: distributions of constant-density snow (0.1 g cm^{-3}) and graupel (0.4 g cm^{-3}) generally melt over a deeper layer than more realistic distributions of snow and graupel having densities that decrease with particle size.

The radiative properties of melting precipitation at microwave frequencies are calculated based upon different methods for describing the dielectric properties of mixed-phase particles. Particle absorption and scattering efficiencies from 10.65 to 85.5 GHz are enhanced greatly for relatively small ($\sim$0.1) meltwater fractions. The relatively large numbers of these partially melted particles just below the freezing level in stratiform regions lead to significant microwave obsorption, exceeding the absorption by rain below the melting layer by factors of 10, 5, 3, and 2 at 10.65, 19.35, 37.0, and 85.5 GHz, respectively, in one test profile. For particles of fixed size, calculated backscatter efficiencies at 13.8 GHz increase in proportion to the particle meltwater fraction, leading to a ''bright band'' of enhanced radar reflectivities in agreement with previous studies.

Radiative properties of the melting layer are sensitive to the choice of dielectric models and the initial water contents and material densities of the ice-phase precipitation particles. In an attempt to resolve these ambiguities in the modeling, four sets of melting profiles are generated based upon two tropical squall-line CRM simulations. The control set contains no mixed-phase precipitation; the other sets include mixed-phase particles with radiative properties determined by different dielectric models and initial particle density distributions. The set of profiles based upon constant-density snow and graupel described by the FS and MGwi dielectric models, respectively, leads to reasonable consistency with PR-derived melting-layer optical depth distributions. Snow and graupel with initial size-dependent densities produce a similar optical depth distribution if the same dielectric models are utilized. A more general conclusion from the intercomparison is that the control profiles that do not contain mixed-phase particles yield op-

tical depths that are systematically lower than those observed. Therefore, the use of the melting-layer model to extend 3D CRM simulations is likely justified, at least until more realistic spectral methods for describing melting precipitation in 3D CRMs are implemented.

Independent in situ measurements of particle size distributions in stratiform regions from airborne probe data have recently been performed as part of the TRMM field campaigns. Coupled with coincident airborne radiometer and radar observations, these data will hopefully lead to a more complete description of the microphysical and radiative properties of melting precipitation. A comparison of modeled and observed melting-layer properties will be the focus of a future investigation by the authors of this study.

In Part II of this series (Olson et al. 2001), the 3D CRM simulations listed in Table 1, augmented by the 1D melting-layer model in stratiform regions, serve as the basis for calculations of upwelling radiances at the TMI frequencies and computations of extinction/reflectivities at the PR frequency.

Acknowledgments. The authors thank Brad Ferrier, Christian Kummerow, Ye Hong, Stephen Lang, and Yansen Wang for their helpful suggestions throughout the course of this study. The research effort was supported by the TRMM Science program.

REFERENCES

Awaka, J., T. Iguchi, and K. Okamoto, 1998: Early results on rain type classification by the Tropical Rainfall Measuring Mission (TRMM) precipitation radar. *Proc. Eighth URSI Commission F Open Symp.*, Aveiro, Portugal, URSI, 143–146.

Bauer, P., J. P. V. Poiares Baptista, and M. Iulis, 1999: On the effect of the melting layer on microwave emission of clouds over the ocean. *J. Atmos. Sci.,* **56,** 852–867.

——, A. Khain, A. Pokrosky, R. Meneghini, C. Kummerow, F. Marzano, and J. P. V. Poaires Baptista, 2000: Combined cloud–microwave radiative transfer modeling of stratiform rainfall. *J. Atmos. Sci.*, **57,** 1082–1104.

Bohren, C. F., and L. J. Battan, 1982: Radar backscattering of microwaves by spongy ice spheres. *J. Atmos. Sci.,* **39,** 2623–2629.

——, and D. R. Huffman, 1983: *Absorption and Scattering of Light by Small Particles*. John Wiley and Sons, 530 pp.

Ebert, E. E., and M. J. Manton, 1998: Performance of satellite rainfall estimation algorithms during TOGA COARE. *J. Atmos. Sci.,* **55,** 1537–1557.

Fabry, F., and W. Szyrmer, 1999: Modeling of the melting layer. Part II: Electromagnetic. *J. Atmos. Sci.,* **56,** 3596–3600.

Ferrier, B., 1994: A double-moment multiple-phase four-class bulk ice scheme. Part I: Description. *J. Atmos. Sci.,* **51,** 249–280.

Flatau, P., G. J. Tripoli, J. Berlinder, and W. Cotton, 1989: The CSU–RAMS cloud microphysics model: General theory and code documentation. Atmospheric Sciences Rep. 451, Colorado State University, Fort Collins, CO, 88 pp.

Haddad, Z. S., E. A. Smith, C. D. Kummerow, T. Iguchi, M. R. Farrar, S. L. Durden, M. Alves, and W. S. Olson, 1997: The TRMM ''Day-1'' radar/radiometer combined rain-profiling algorithm. *J. Meteor. Soc. Japan,* **75,** 799–808.

Kummerow, C., 1998: Beamfilling errors in passive microwave rainfall retrievals. *J. Appl. Meteor.,* **37,** 356–370.

Liao, L., and R. Meneghini, 2000: Investigation of the dielectric constants of inhomogeneous air–ice and snow–water spheres. *Proc. IEEE 2000 Int. Geoscience and Remote Sensing Symp.*, Honolulu, HI, IEEE, 1804–1806.

——, ——, and T. Iguchi, 1999: Simulations of mirror image returns of air/space-borne radars in rain and their applications in estimating path attenuation. *IEEE Trans. Geosci. Remote Sens.,* **37,** 1107–1121.

Lin, Y.-L., R. D. Farley, and H. D. Orville, 1983: Bulk parameterization of the snow field in a cloud model. *J. Climate Appl. Meteor.,* **22,** 1065–1092.

Locatelli, J. D., and P. V. Hobbs, 1974: Fall speeds and masses of solid precipitation particles. *J. Geophys. Res.,* **79,** 2185–2197.

Maxwell-Garnett, J. C., 1904: Colors in metal glasses and in metallic films. *Philos. Trans. Roy. Soc. London,* **203A,** 385–420.

Meneghini, R., and L. Liao, 1996: Comparisons for cross sections for melting hydrometeors as derived from dielectric mixing formulas and a numerical method. *J. Appl. Meteor.,* **35,** 1658–1670.

——, and ——, 2000: Effective dielectric constants of mixed-phase hydrometers. *J. Atmos. Oceanic Technol.,* **17,** 628–640.

——, T. Iguchi, T. Kozu, L. Liao, K. Okamoto, J. A. Jones, and J. Kwiatkowski, 2000: Use of the surface reference technique of path attenuation estimates from TRMM precipitation radar. *J. Appl. Meteor.,* **39,** 2053–2070.

Mitchell, D. L., R. Zhang, and R. L. Petter, 1990: Mass-dimensional relationships for ice particles and the influence of riming on snowfall rates. *J. Appl. Meteor.,* **29,** 153–163.

Mugnai, A., H. J. Cooper, E. A. Smith, and G. J. Tripoli, 1990: Simulation of microwave brightness temperatures of an evolving hailstorm at SSM/I frequencies. *Bull. Amer. Meteor. Soc.,* **71,** 2–13.

Olson, W. S., P. Bauer, C. D. Kummerow, Y. Hong, and W.-K. Tao, 2001: A melting-layer model for passive/active microwave remote sensing applications. Part II: Simulations of TRMM observations. *J. Appl. Meteor.,* **40,** 1164–1179.

Panegrossi, G., and Coauthors, 1998: Use of cloud model microphysics for passive microwave-based precipitation retrieval: Significance of consistency between model and measurement manifolds. *J. Atmos. Sci.,* **55,** 1644–1673.

Rutledge, S. A., and P. V. Hobbs, 1983: The mesoscale and microscale structure and organization of clouds and precipitation in midlatitude cyclones. VIII: A model for the ''seeder-feeder'' process in warm-frontal rainbands. *J. Atmos. Sci.,* **40,** 1185–1206.

——, and ——, 1984: The mesoscale and microscale structure and organization of clouds and precipitation in midlatitude cyclones. XII: A diagnostic modeling study of precipitation development in narrow cold-frontal rainbands. *J. Atmos. Sci.,* **41,** 2949–2972.

Schols, J., J. Haferman, J. Weinman, C. Prabhakara, M. Cadeddu, and C. Kummerow, 1997: Polarized microwave radiation model of melting deformed hydrometeors. Preprints, *Ninth Conf. on Atmospheric Radiation,* Long Beach, CA, Amer. Meteor. Soc., 270–273.

Smith, E. A., C. D. Kummerow, and A. Mugnai, 1994: The emergence of inversion-type precipitation profile algorithms for estimation of precipitation from satellite microwave measurements. *Remote Sens. Rev.,* **11,** 211–242.

Tao, W.-K., and J. Simpson, 1993: Goddard Cumulus Ensemble model. Part I: Model description. *Terr. Atmos. Oceanic Sci.,* **4,** 35–72.

Tripoli, G. J., 1992a: A nonhydrostatic model designed to simulate scale interaction. *Mon. Wea. Rev.,* **120,** 1342–1359.

——, 1992b: An explicit three-dimensional nonhydrostatic numerical simulation of a tropical cyclone. *Meteor. Atmos. Phys.,* **49,** 229–254.